Article

Increased melt from Greenland's most active glacier fuels enhanced coastal productivity

Check for updates

Michael Wood [1] ✉, Dustin Carroll [1,2], Ian Fenty [2], Clément Bertin [2], Basil Darby[1], Stephanie Dutkiewicz[3], Mark Hopwood [4], Ala Khazendar [2], Lorenz Meire [5], Hilde Oliver [6], Tara Parker [1] & Josh Willis [2]

Seasonal phytoplankton blooms in Greenland's coastal waters form the base of marine food webs and contribute to oceanic carbon uptake. In Qeqertarsuup Tunua, West Greenland, a secondary summertime bloom follows the Arctic spring bloom, enhancing annual primary productivity. Emerging evidence links this summer bloom to subglacial discharge from Sermeq Kujalleq, the most active glacier on the Greenland Ice Sheet. This discharge drives localized upwelling that may alleviate nutrient limitation in surface waters, yet this mechanism remains poorly quantified. Here, we employ a high-resolution biogeochemical model nested within a global state estimate to assess how discharge-driven upwelling influences primary productivity and carbon fluxes. We find that upwelling increases summer productivity by 15–40% in Qeqertarsuup Tunua, yet annual carbon dioxide uptake rises by only ~3% due to reduced solubility in plume-upwelled waters. These findings suggest that intensifying ice sheet melt may alter Greenland's coastal productivity and carbon cycling under future climate scenarios.

Qeqertarsuup Tunua (English: Disko Bay), West Greenland, is home to several large marine-terminating glaciers including Sermeq Kujalleq (SK) in Kangiata Sullua near the town of Ilulissat, as well as Eqip Sermia, Kangilernata Sermia, Kujalleq, and Sermeq Avannarleq in the Torsukattak fjord system (Fig. 1). SK is the largest glacier in the region and one of the most prolific in Greenland: its annual 40 Gt yr^{-1} of ice flux is the highest of all glaciers flowing from the ice sheet[1] and its 78,000 km^2 hydrological drainage basin is the third largest behind Nioghalvfjerdsfjorden and Zachariae Isstrøm in the Northeast Greenland Ice Stream[1]. Each summer, meltwater from the ice sheet within SK's basin is routed through subglacial hydrological pathways and discharged at the roughly 850-m deep grounding line, with an average summertime freshwater flux of more than 1200 m^3 per second[2]. As this fresh, buoyant subglacial discharge rises (Fig. 1c), the resulting turbulent plume entrains deep water masses in the fjord basin[3], amounting to an estimated total upwelling flux of more than 45,000 m^3 s^{-1} — nearly 40-fold higher than the discharge alone and the highest of any Greenland glacier[2]. Similar to other upwelling systems around the global ocean, this vertical flux results in a transport of nitrate from depth into the photic zone[4,5]. Since nitrate is a limiting nutrient for primary productivity in

Qeqertarsuup Tunua, as is broadly the case in the Arctic and coastal regions of the North Atlantic[6], this delivery of nitrate has been hypothesized to alleviate summertime nutrient limitation for phytoplankton growth[5,6].

In northern Qeqertarsuup Tunua in the Sullorsuaq Strait, remotely-sensed chlorophyll-*a* (Chl-a) observations show two annual maxima: one in April and another in August (Fig. 2a). The first peak in April (Fig. 2a) is associated with the break up of sea ice and increase of solar radiation in spring (Fig. 2c) that is consistently observed across the Arctic[7]. The second peak in August correlates with the timing of the meltwater season (Fig. 2b) and is consistent with predictions from idealized plume models that suggest subglacial discharge may be alleviating nutrient limitation in this region[8]. While fall blooms have been previously observed[9,10] and modeled[11] in the Arctic, their mechanism has largely been linked to the delayed formation of sea ice and enhanced vertical mixing during fall, not ice-sheet discharge. Given that ice-sheet melt and associated meltwater runoff are projected to increase in the coming decades[12], SK and other large Greenland glaciers may be poised to enhance the secondary summertime peak in productivity and induce widespread changes in coastal ecosystems with potential downstream impacts on fisheries, marine mammals, and carbon cycling.

[1]Moss Landing Marine Labs, San José State University, San José, CA, USA. [2]Jet Propulsion Laboratory, California Institute of Technology, Pasadena, CA, USA. [3]Massachusetts Institute of Technology Cambridge, Cambridge, MA, USA. [4]Department of Ocean Science and Engineering, Southern University of Science and Technology, Shenzhen, China. [5]Greenland Climate Research Centre, Greenland Institute of Natural Resources, Nuuk, Greenland. [6]Woods Hole Oceanographic Institution, Woods Hole, MA, USA. ✉e-mail: mike.wood@sjsu.edu

Fig. 1 | Extents of model domains used in this study. a Domain of the L1 regional model resolving northward transport in the West Greenland Current (WGC) to Qeqertarsuup Tunua. Global inset shows location of the L1 regional model in the context of the global-ocean ECCO-Darwin domain. **b** Domain of the L2 fjord-scale model of Qeqertarsuup Tunua and the Kangiata Sullua and Torsukattak fjord systems. The extent of the L2 domain within L1 is shown in the orange polygon in panel **a**. The black polygon encompassing the Sullorsuaq Strait is used to sample model results upstream of the glacier outlets. **c** Geometry of Kangiata Sullua with Sermeq Kujalleq (SK) on the right. The pink shading represents the concentrations of nutrients (nitrate, phosphate, and silica) within the fjord system with low nutrient concentrations in the photic zone and elevated nutrients at depth.
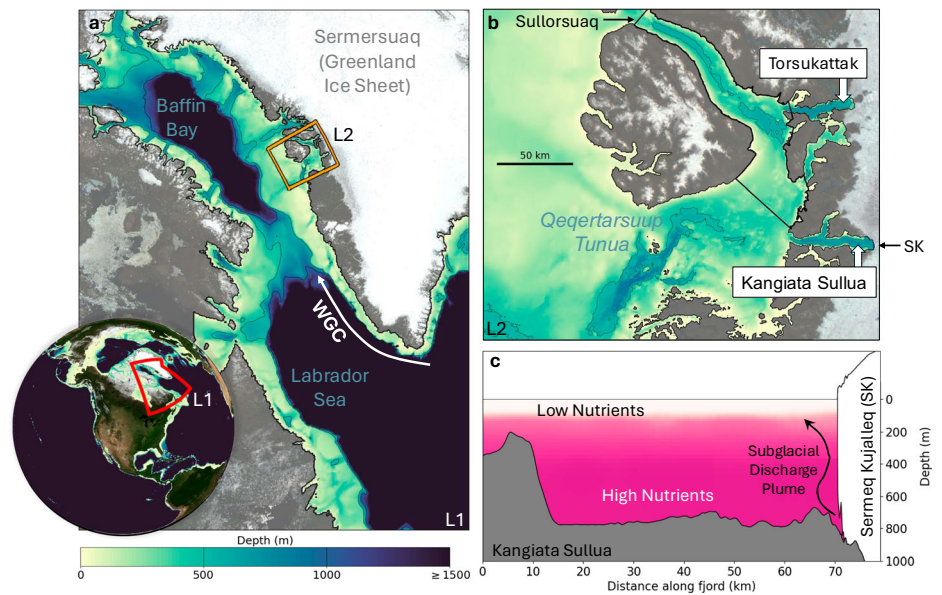
Fig. 2 | Observed properties in Sullorsuaq Strait highlighted during model years. a Spatially-averaged Chl-a concentration in the Sullorsuaq Strait from remotely-sensed estimates (OC-CCI V6). The years 2008, 2012, 2017, and 2019 (shown as colored lines) correspond to observations during specific years in our Qeqertarsuup Tunua simulations. The observed lines have been smoothed with a 7-day Hann window and interpolated to fill observational gaps. The gray envelope represents one standard deviation from the time-mean Chl-a concentration during 2000–2020. **b** Subglacial discharge volume flux into Qeqertarsuup Tunua from SK and four glaciers in the Torsukattak region. **c** Median sea-ice concentration in Qeqertarsuup Tunua estimated from passive microwave remote-sensing measurements.
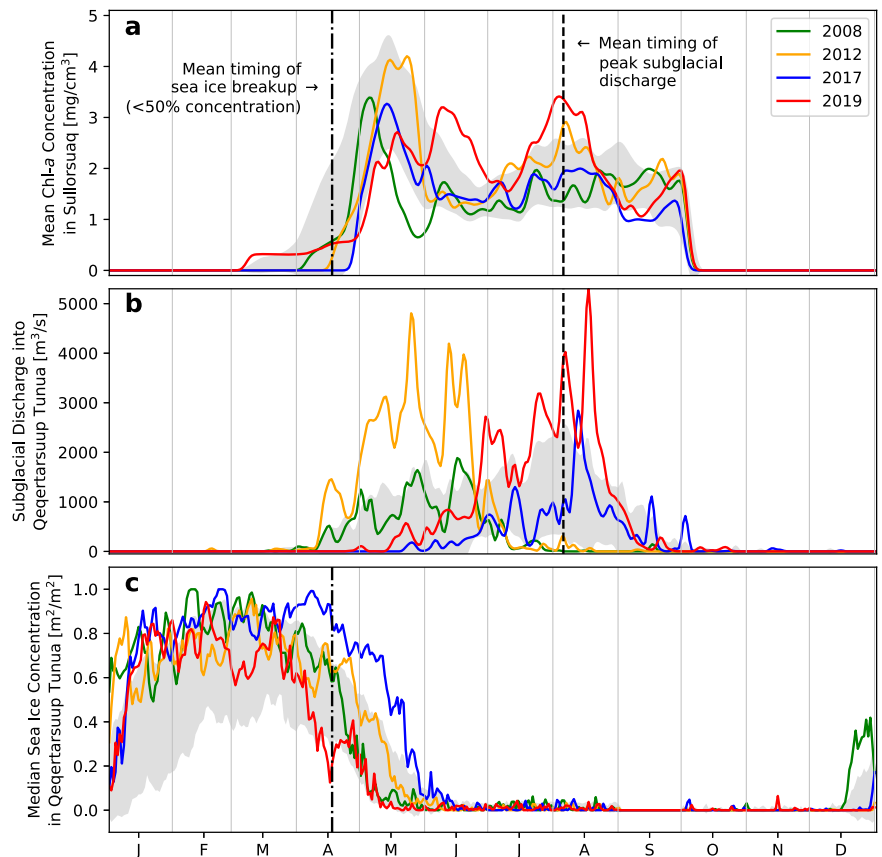
From an observational perspective, the effect of subglacial discharge on nutrient upwelling and productivity has been previously observed in a few Greenland fjord systems: Nuup Kangerlua, a fjord in southwest Greenland where three large glaciers terminate[13–15]; Sermilik fjord, where the large Helheim glacier terminates[4]; and in Inglefield Gulf, northwest Greenland, near the terminus of Bowdoin glacier[16]. Most recently, nutrient measurements from Qeqertarsuup Tunua indicate strong links between subglacial discharge and nutrient concentrations in the photic zone[17]. However, outside of these regions, in-situ observations of nutrient and Chl-a concentrations linking glacier melt to productivity remain extremely sparse, with many fjords lacking any observations. From a modeling perspective, idealized models have suggested that the links between plume-driven upwelling, nutrient availability[8], and primary productivity are widespread around Greenland[5,6]; A few high-resolution coupled physical-

biogeochemical models that provide a mechanistic context for these connections have begun to be developed[18,19], although to date, they have been designed as process-based models which do not resolve interannual variability or have lacked realistic representation of subglacial discharge plume dynamics. This inhibits the attribution of observed changes in primary productivity to coupled ice-ocean-biological processes, especially in regions that lack in-situ measurements.

Here, we aim to broaden our understanding of nutrient upwelling and the associated response of primary productivity using a high-resolution coupled physical-biogeochemical model of Qeqertarsuup Tunua that includes realistic phytoplankton ecology and associated bloom phenology. To connect our fjord-scale simulations to physical and biogeochemical drivers in the global ocean, we leverage a nested model framework[20] to link our model with ECCO-Darwin — a data-assimilative global-ocean biogeochemistry model[21,22] from the Estimating the Circulation and Climate of the Ocean (ECCO) consortium. In the nested framework, we first use conditions from the 1/3° resolution ECCO-Darwin model to construct a 1/12°-resolution regional model to resolve nutrient transport via the West Greenland current (WGC) and into Qeqertarsuup Tunua (Fig. 1a) during years 1992–2021. Subsequently, we use our regional model to construct a 500 m resolution, fjord-scale model (Fig. 1b) that resolves circulation within Qeqertarsuup Tunua as well as in the adjacent Kangiata Sullua and Torsukattak fjord systems. Within the fjords, glaciers are implemented using an online plume model that estimates submarine melt and upwelling resulting from subglacial discharge[23]. We assess our model results by comparing with a suite of in situ and remotely-sensed observational data for nutrient and Chl-a concentrations, sea ice, and physical oceanographic data. These data include temperature and salinity profiles from two autonomous floats we deployed in Qeqertarsuup Tunua, offering rare wintertime measurements of water-mass transformations that have not been historically observed in the area. Further details regarding our modeling approach and the comparison to observations are found in the Methods.

Given the high computational cost of the fjord-scale model with biogeochemistry, we focus on 4 years with distinct ice-sheet melt signatures — two high-melt years (2012, 2019) and two low-melt years (2008, 2017) (Fig. 2b). In 2008 and 2012, surface melt peaked relatively early in the melt season around 1 June, while in 2017 and 2019 it peaked later around 1 August, yielding temporal differences between sets of high- and low-discharge scenarios (Fig. 2b). After establishing our experiment with the subglacial discharge plume, we then examine the effect of the plume on biological activity and ocean carbon uptake (henceforth referred to as carbon uptake) with a suite of sensitivity experiments. First, to isolate the effect of subglacial discharge, we run our model in each year without the plume implementation to quantify discharge-driven changes in nutrient concentrations and primary productivity. Then, to determine the relative effect of physical versus biological drivers of carbon uptake in Qeqertarsuup Tunua, we run our model without primary producers, i.e., with physical and chemical constituents only. These experiments allow us to compare the relative effects of biological carbon fixation on carbon uptake in simulations with and without the plume (see Methods). Besides these changes, all other model parameters, such as initial conditions, boundary conditions, and external forcing, are kept the same.

Results

To assess the results of our model experiments, we first focus on the impact of the subglacial discharge plume on nutrient availability in the photic zone by comparing model results with and without the plume implementation. We place particular emphasis on the Sullorsuaq Strait (Fig. 1a), downstream of the glacier outlets, which hosts a summertime bloom hotspot. Subsequently, we examine the effect of nutrient concentration differences on Chl-a and primary productivity. Finally, we examine differences in carbon uptake in Qeqertarsuup Tunua resulting from plume activity, quantifying the differences between physical and biological processes by comparing model results with and without primary producers.

Nutrients

Before the onset of ice-sheet melt, nitrate concentrations in the upper ocean in both sets of model experiments are similar. At a depth of 20 m, chosen as an approximate middle depth of the photic zone, nitrate increased from 1–2 μM in January to 3–4 μM in March (Supplementary Fig. 1). This increase in nutrients in the surface-ocean layer results from the net effect of vertical mixing, advective transport, and lack of biological consumption due to reduced solar radiation. As the season progresses through spring, nitrate concentrations increase at similar rates through May, although the simulations with glacier forcing begin to bifurcate: simulations with subglacial discharge yield higher levels of nutrient concentrations relative to those without (Fig. 3). We note that these differences even occur in April 2017 and 2019, when subglacial discharge is very low (Fig. 2b).

Inter-model differences become particularly apparent as solar radiation increases, sea ice starts to break up, and ice-sheet melt drives vigorous rates of subglacial discharge and upwelling. In 2008 and 2012, years with earlier peaks in subglacial discharge, nitrate was higher by 3–4 μM (Fig. 3b). Vertical profiles demonstrate that these differences are primarily confined to depths between 0–100 m, which are largely within the photic zone (Fig. 3b). These elevated concentrations emanate from their upwelling source in glacier plume regions, where high concentration differences are observed. For example, near SK, nitrate is elevated by up to 9 μM in summer in the plume region (Supplementary Figs. 2 and 3), which is consistent with observations[17]. At depths below approximately 300 m, there are negligible differences between model runs i.e. nitrate supplies are maintained at the depths where large rates of entrainment occur in subglacial discharge plumes.

Elevated levels of nitrate persist in 2008 and 2012 through July until all nitrate in the photic zone is consumed (Supplementary Fig. 1) and productivity ceases. In contrast to years 2008 and 2012, 2017 and 2019 experience peak discharge later in the season and thus have elevated levels of nitrate during late summer (Fig. 3). The differences in phosphate and silica between model experiments — other macronutrients critical for productivity — follow a similar annual progression as the nitrate: each have elevated concentrations in the photic zone in the months following the onset of subglacial discharge (Supplementary Fig. 4). Again, elevated levels of both nutrients are observed earlier in the season for 2008 and 2012 compared to 2017 and 2019, demonstrating of the role of glaciers in upwelling nutrients to the photic zone. Similar to nitrate, both phosphate and silica concentrations decline during the months of May, June, and July during months of peak productivity — although neither are completely consumed, consistent with the hypothesis that nitrate is the limiting nutrient for productivity in this region. Phosphate remains above 0.2 μM in all simulations while silica remains within 6–8 μM (Supplementary Fig. 1).

Productivity

The effect of the glacier upwelling plume on productivity in Qeqertarsuup Tunua is directly evident by comparing spatial maps of Chl-a concentration after the peak subglacial discharge of each year (Fig. 4). In simulations without subglacial discharge, summertime Chl-a concentrations remain biased low compared to observations, especially near the glacier fjords. For example, at a depth of 20 m, Chl-a concentrations remain within 1–2 mg m^{-3} and are largely homogeneous throughout the bay. In contrast, simulations that include subglacial discharge plumes yield much higher Chl-a concentrations that peak around 5–6 mg m^{-3} — especially in the Sullorsuaq region downstream of Sermeq Kujalleq and the other four major glaciers that terminate into Qeqertarsuup Tunua. The increased Chl-a values occur downstream from the glacier outlets as there are relatively strong down-fjord currents of 0.1–0.3 m s^{-1} in the upper 200 m of the water column. Further, there is a several-day time-lag between increased nutrients and peak Chl-a concentration due to nutrient uptake rates. These patterns are broadly consistent with both the magnitude and spatial distribution of remotely-sensed Chl-a from the Ocean Colour Climate Change Initiative Version 6 project (OC-CCI, Fig. 4c, f, i, l) as well as with in-situ measurements of Chl-a collected during 2022[17] (Supplementary Fig. 5). Temporally,

Fig. 3 | Effect of subglacial discharge on nitrate concentrations in Sullorsuaq Strait. a Temporal differences in nitrate concentrations at 20 m depth in the Sullorsuaq Strait between the model simulations with the plume and those without. Nitrate concentrations are spatially averaged in the polygon encompassing Sullorsuaq, as shown in Fig. 1. **b** Differences in space-time-mean profiles of nitrate concentration in Sullorsuaq between model simulations with and without the plume. Space-time means are computed from 15 July to 15 August for each model grid cell in the Sullorsuaq polygon at each model depth level.
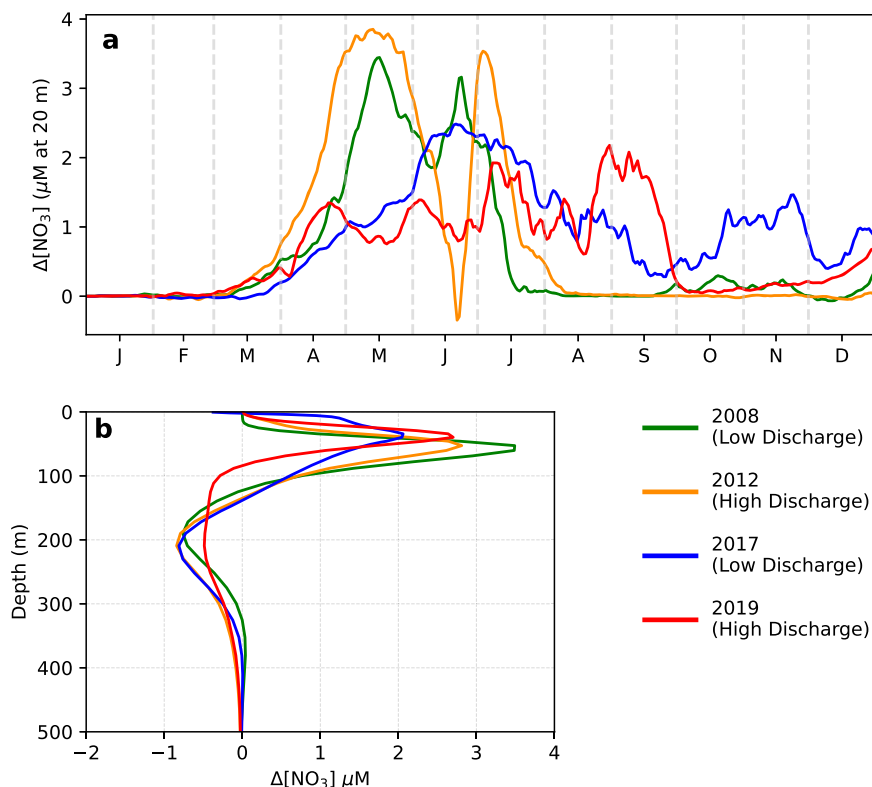
increased Chl-a concentrations are observed during May through October (Fig. 5a and Supplementary Fig. 5). The differences in spatially-integrated net Chl-a between the two model runs reach maxima around 1 July in 2008 and 2012 and later around 1 August in 2017 and 2019, consistent with the timing of subglacial discharge from the marine-terminating glaciers and the persistence of elevated nutrient levels through the summer (Fig. 5a).

The differences in Chl-a between simulations with and without glacier forcing also differ by phytoplankton functional groups (Supplementary Fig. 6). Without the plume, the phytoplankton community largely consists of non-diatom large eukaryotes, which experience small blooms after the breakup of sea ice each year, reaching a peak in Chl-a biomass of 1–1.5 mg m^{-3}. The only exceptions are small plumes of diatoms after the sea ice break-up in 2012 and 2019 (<0.1 mg m^{-3} Chl-a), a small late-season bloom of diatoms in 2017 (<0.05 mg m^{-3} Chl-a), and a small bloom of picoeukaryotes that occurs in later 2017 (<0.03 mg m^{-3} Chl-a). When the discharge plume is active, both non-diatom eukaryotes and diatoms groups enhance the productivity signal, with peak Chl-a concentrations of 1.5–2.5 mg m^{-3} and 0.2–0.4 mg m^{-3}, respectively. In 2012 and 2019, the high discharge years, there are further contributions from both picoeukaryotes and picocyanobacteria, although in quantities that are approximately an order of magnitude less than eukaryotes.

In all simulations, light is the limiting factor for productivity during December through May due to widespread sea ice cover and limited solar radiation. These months are characterized by limited productivity and an increase in nutrient concentrations in the upper-100 m of the water column. As sea-ice cover declines, productivity commences, and nutrients are rapidly consumed until nitrate is drawn down close to 0 μM in the surface layer. This consumption of nitrate is consistent with the general expectation that nitrate is the main proximal limiting nutrient[6], although diatoms in the Arctic have been observed to become silica limited before nitrate is drawn down[24]. As a result of elevated levels of nitrate, productivity extends later in the year in the simulations with subglacial discharge.

The differences in Chl-a observed in the photic zone (Fig. 5a) are associated with higher rates of primary productivity (Fig. 5b). The

Sullorsuaq Strait, downstream of the glaciers, is a hot spot of productivity when the subglacial discharge plume is activated (Supplementary Fig. 7). In all experiment years, total annually-integrated primary productivity approximately doubles when the discharge plume is enabled (Supplementary Table 1), with the largest increase of +158% in 2012. The higher primary productivity difference in 2012 is primarily associated with the earlier onset of productivity observed in all phytoplankton functional groups (Supplementary Fig. 6). When averaged across the entire Qeqertarsuup Tunua domain, we again find the highest increase in primary productivity associated with glacier forcing in the year 2012 (Fig. 5b), peaking at 20 GgC per day. Integrated over the year and spatially averaged across Qeqertarsuup Tunua, total primary productivity increased from 31 gC m^{-2} yr^{-1} to 43 gC m^{-2} yr^{-1} (+40%) in the simulation with the discharge plume. In 2008, 2017, and 2019, the increases were around 20% (Supplementary Table 1).

Ocean Carbon Uptake

For the months of May through December, there is an uptake of CO_2 in Qeqertarsuup Tunua when waters are ice free (Supplementary Fig. 8). This uptake is the combined result of biological and physical processes, which are largely separated by season. During summer, the biological fixation of carbon by primary producers during summer decreases dissolved inorganic carbon (DIC) concentrations, which then lower surface-ocean pCO$_2$ and increase ocean carbon uptake, while cooling of surface-ocean waters in Qeqertarsuup Tunua during winter increases the solubility of CO_2 at the ocean surface (Supplementary Fig. 9). To isolate and quantify these distinct effects in space and time, we compare model results with and without primary producers (see Methods, Fig. 6, Supplementary Figs. 10 and 11). During the summer, CO_2 uptake is driven by primary productivity while solubility driven by plume upwelling contributes to the outgassing of CO_2 (Fig. 6). Starting at the end of September, however, surface-ocean temperatures begin to cool and solubility of surface-ocean CO_2 increases, resulting in elevated uptake compared to summer rates (Supplementary Fig. 11). In contrast, productivity during these months declines so that CO_2 uptake is driven mostly by physical rather than biological processes. Overall,

Fig. 4 | Comparison of chlorophyll-a in Qeqer-tarsuup Tunua from models and remotely-sensed estimates. Chl-a concentrations in 2008 from **a** the model without glaciers, **b** the model with glaciers, and **c** the OC-CCI V6 Chl-a product[55]. Temporal means are computed over 30 days in the months indicated on the left axis. Model Chl-a is taken at 20 m depth. Rows with panels **d–f**, **g–i**, **j–l** are identical for years 2012, 2017, and 2019, respectively.
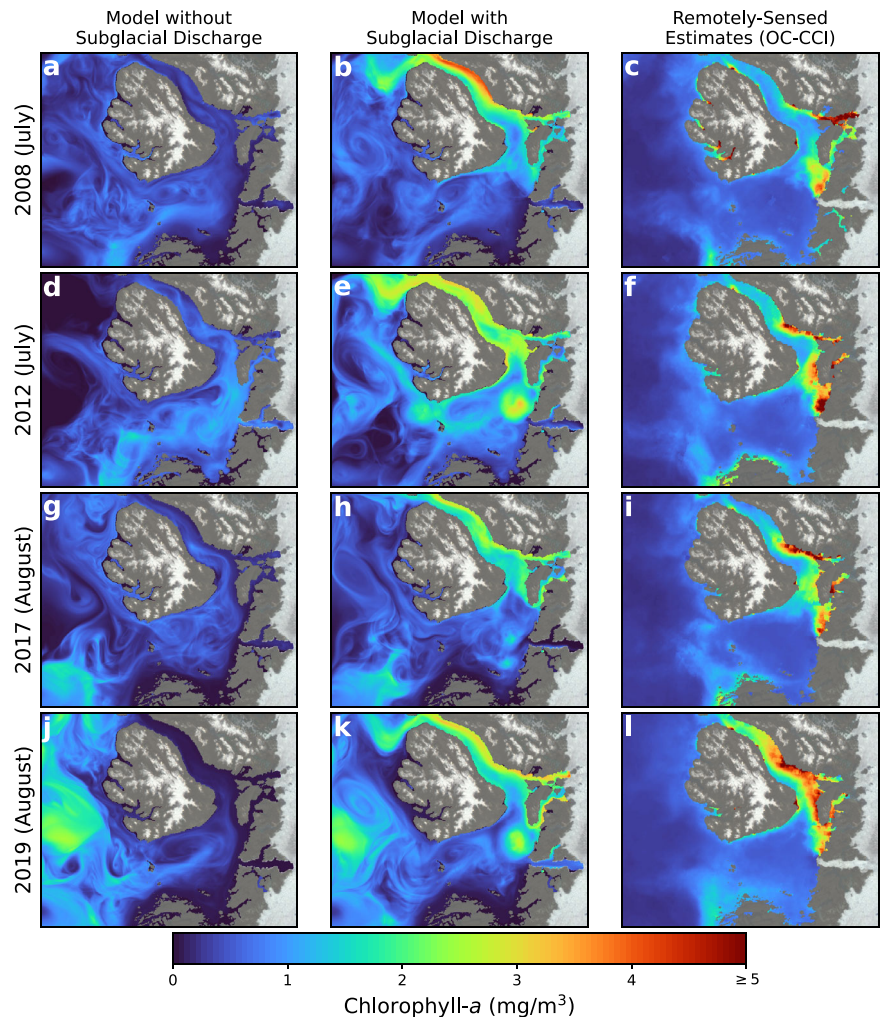
when integrated through the entire year, physical processes account for 65–75% of CO_2 uptake, while biological fixation accounts for the remainder (Supplementary Fig. 11).

In simulations with subglacial discharge, we observe the influence of the plume on CO_2 uptake in both physical and biological processes. For all model years during summer (Fig. 6), we observe a decline in CO_2 uptake associated with upwelling of warm, DIC-rich waters from the discharge plume that results in a seasonal outgassing of CO_2. In contrast, the model simulations reveal an increase in CO_2 uptake associated with productivity that offsets this effect. Despite the noticeable summertime difference induced by primary producers, annually-integrated CO_2 uptake in Qeqer-tarsuup Tunua is similar with and without the discharge plume, increasing modestly about 1–2 gC m^{-2} yr^{-1}, or about 3% over background rates (Fig. 5c). In 2012, the year with the highest increase in plume-driven productivity, the increase in CO_2 uptake is largely driven by enhanced biological carbon fixation (Supplementary Fig. 11). In contrast in 2017, the year with the lowest increase in productivity, changes in solubility had the largest effect on CO_2 uptake and there was an overall net negative effect on CO_2 uptake.

Discussion

From the results of our model experiments, we find that glacier forcing has a considerable impact on nutrient availability and primary productivity in Qeqertarsuup Tunua. Futhermore, subglacial discharge has a direct influence on nitrate concentrations in the photic zone and it should be noted that subglacial discharge itself is not a nutrient source. In other words, the increase in nitrate concentration is driven by plume-driven entrainment and

upwelling of fjord bottom waters rather than lateral fluxes from terrestrial systems. Our simulations with subglacial discharge also generally replicate the magnitude and spatiotemporal patterns of remotely-sensed summertime Chl-a, especially in waters downstream of outlet glaciers, while simulations without glaciers do not reproduce those patterns. The increase and subsequent decline in productivity in conjunction with changes in nitrate concentrations in all experiments also supports the expectation that this region is nitrate-limited: productivity persists longer into summer in simulations with subglacial discharge (Fig. 5) until nitrate in the photic zone again reaches zero (Supplementary Fig. 1). This is consistent with earlier work showing nitrate limitation in West Greenland[6,13,14]. Further, since there are still several months in which nitrate concentrations are near-zero each year, additional nitrate associated with further increases from subglacial discharge have the potential to fuel continued increases in productivity.

In all experiment years, the plume-driven increase of nutrients in the photic zone yields higher summertime Chl-a concentrations relative to simulations without glacier plumes, reflective of higher rates of primary productivity. While this additional productivity contributes to enhanced air-sea CO_2 flux during the summertime, the gains are largely offset by changes in solubility, such that cumulative CO_2 uptake in Qeqertarsuup Tunua increases only modestly by approximately 3% over simulations with no or low discharge (Fig. 5). By the end of the century, regional climate models project a 100–300% increase in ice-sheet runoff through englacial hydrological systems[25], which would fuel enhanced subglacial discharge at glacier terminus locations. The results of our simulations suggest that Qeqertarsuup Tunua, as well as other coastal regions near other large Greenland outlet glacier systems, could experience enhanced summertime

Fig. 5 | Effect of subglacial discharge on productivity and carbon dioxide uptake in Qeqertarsuup Tunua. Temporal differences in **a** Chlorophyll-a concentration, **b** primary productivity, and **c** cumulative CO_2 uptake between simulations with and without discharge in years 2008, 2012, 2017, and 2019. Chlorophyll-a is sampled at 20 m depth and spatially averaged across the Qeqertarsuup Tunua (L2) domain. Primary productivity is integrated across all depths and then across the Qeqertarsuup Tunua (L2) domain. CO_2 uptake is the net air-sea CO_2 flux integrated across the domain. The cumulative difference refers to total integrated air-sea CO_2 flux into the ocean between simulation with and without subglacial discharge.
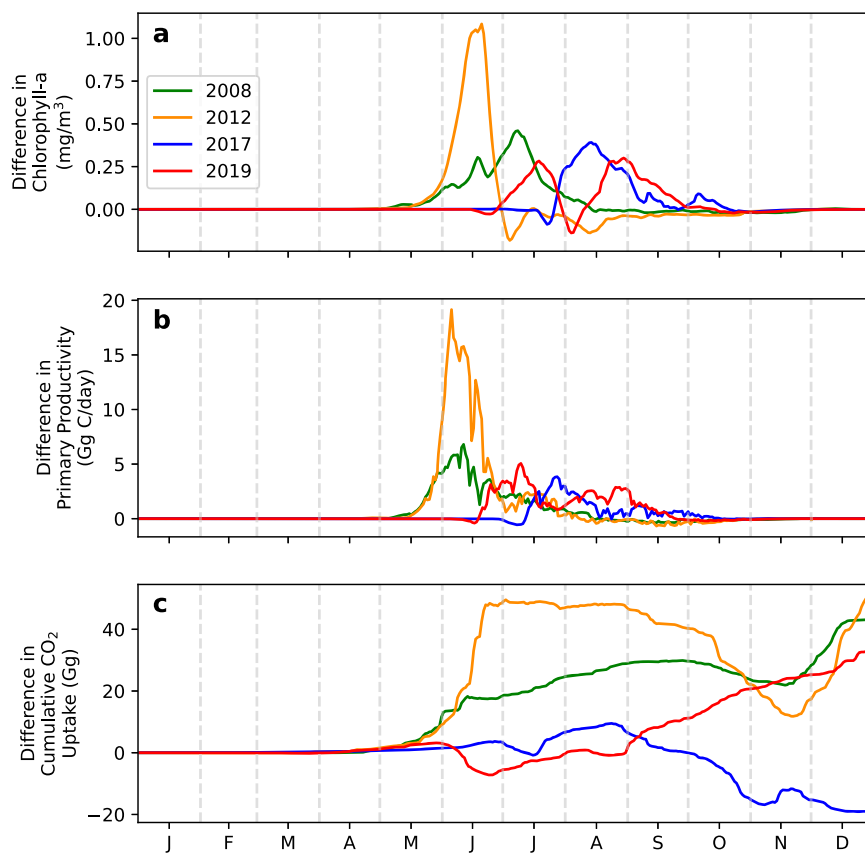

productivity in the coming years. However, if the compensatory relationship between solubility and biological activity described above persists, this additional activity is not expected to contribute substantially to an enhanced sink of carbon dioxide into the ocean.

The magnitude and spatial extent over which the subglacial discharge plume increases primary productivity in our models is quite different from the results of a similar model from Møller et al. 2023[18]. The primary difference leading to this discrepancy can be attributed to the parameterized treatment of subglacial discharge. In our model, subglacial discharge emanates from glacier-adjacent cells with grounding line depths of 600–800 m and is implemented with the online-coupled *iceplume* model[23]; in contrast, the main results from Møller et al. (2023) rely on simulations in which the subglacial discharge is distributed into the surface layer of the ocean only or at shallow depths, and lack the critical effect of plume-driven entrainment and upwelling. Due to this implementation, the concentration of ambient nutrients entrained into the upwelling plume as well as the volumetric entrainment rate are lower compared to our results, diminishing the simulated effect of upwelling on nutrient concentrations in the photic zone and the overall response of primary productivity[6]. These differences in model implementation underscore the importance of the subglacial discharge plume signal in modulating nutrient concentrations and productivity in our model.

While our model reproduces many of the observed spatiotemporal hydrographic and biogeochemical patterns in Qeqertarsuup Tunua (see Model Evaluation against Observations section in Methods), we note several differences between our model and observations in Qeqertarsuup Tunua and discuss here how they impact the interpretation of our results. First, the simulated nitrate levels at depths greater than 100 m are biased low by 3–5 μM relative to available World Ocean Atlas observations from 2004 to 2017 (Supplementary Fig. 12). Since nitrate concentrations at depth are entrained in the subglacial discharge plumes and upwelled into the photic zone, lower concentrations of deep nitrate would induce a low bias in photic zone concentrations. Nonetheless, our profiles of nitrate in the photic zone

are still generally comparable in magnitude to observations (Supplementary Fig. 12). Second, sea ice in our model persists too long in spring and reforms too early in the fall (Supplementary Fig. 13). Since sea ice inhibits downwelling solar radiation into the ocean, this delays the spring bloom in all of our simulations. While the timing of productivity is thus shifted later in the year, we do not expect this to influence the total productivity because nitrate in the photic zone is consumed in all simulations (Supplementary Fig. 1). Furthermore, we do not expect this to impact our quantification of the effect of subglacial discharge since ice-sheet runoff largely peaks later in the season when sea ice has already broken up and melted (Fig. 2). Third, our model does not include a representation of turbidity, which may result in light limitation being biased low in shallow regions or in locations near discharge outlets where sediment signals are large[26]. However, turbidity observations suggest particle plumes are generally limited to within a few kilometers of glacier termini at the surface and rapidly sink[27] resulting in an exponential decline in sedimentation with increasing distance downstream of tidewater glaciers[27], limiting this influence outside of the fjords in Qeqertarsuup Tunua. Fourth, our model does not contain icebergs, which may have an impact on productivity. On one hand, icebergs may inhibit productivity in the ice-choked Kangiata Sullua and Torsukattak fjords by limiting photosynthetically-available radiation; on the other hand, icebergs may modulate nutrient concentrations in the photic zone either as a direct source[28] or potentially through the upwelling of nutrients in ambient melt plumes[29]. While the effects of icebergs are not present in our simulations, we would expect their effect to be similar with and without the subglacial discharge and thus have a negligible effect on our results pertaining to discharge in particular. The influence of icebergs on productivity in Greenland remains an open question and further studies are needed to investigate their effect in fjords across Greenland, especially in the case of localized upwelling, which is challenging to observe due to the rapid dilution of fine-scale iceberg meltwater plumes. Finally, our model is set-up with a *darwin* ecosystem that is optimized for the global ocean rather than for Arctic- or Greenland-specific conditions. Analogous to issues with biases in

Fig. 6 | Summertime partitioning of ocean carbon dioxide uptake between physical and biological processes. Spatial differences in cumulative CO_2 flux during the summer month following peak discharge partitioned by the following sources: **a** baseline air-sea CO_2 flux in the absence of primary productivity or the subglacial discharge plume, **b** the effect of the subglacial discharge plume on CO_2 flux in the absence of primary productivity, **c** CO_2 flux resulting from primary productivity, and **d** CO_2 flux resulting from plume-induced changes in primary productivity. The first row **a**–**d** corresponds to a month in summer 2008 following the peak of primary productivity. Rows for **e**–**h**, **i**–**l**, **m**–**p** are identical for 2012, 2017, and 2019. Timeseries of spatially-integrated air-sea CO_2 flux throughout the year are shown in Supplementary Fig. 11.
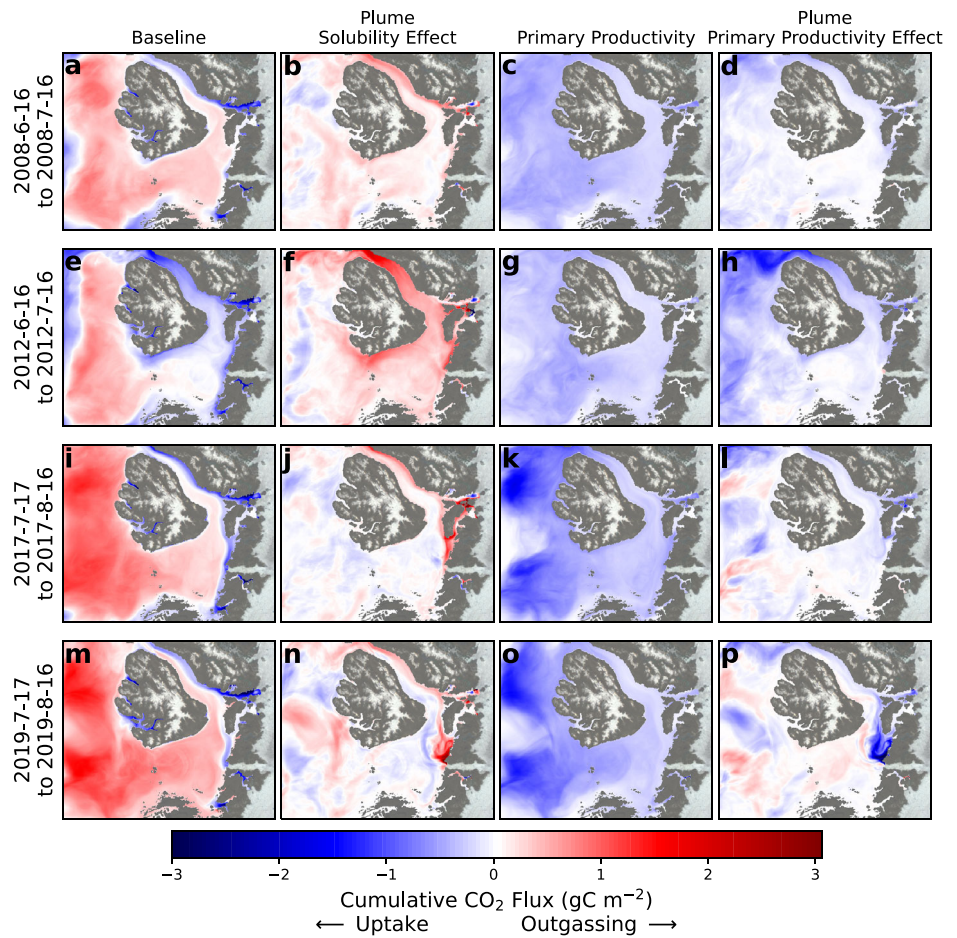
remotely-sensed estimates of Chl-a, an ecosystem model developed for global-ocean conditions yet applied to coastal Greenland may misrepresent the magnitude and/or community composition of phytoplankton.

Despite these caveats, our simulations nonetheless reproduce a wide array of physical and biogeochemical observations, bolstering confidence in conclusions regarding the effect of subglacial discharge on productivity, now and in the future. Furthermore, our simulations provide supporting evidence that high-latitude double blooms can be driven by ice-sheet discharge, which is another mechanism alongside delayed sea-ice formation during fall and associated enhanced vertical mixing of nutrients[10]. As ice-sheet meltwater increases in coming decades, the results of this study suggest that primary productivity near marine-terminating glaciers with deep grounding lines will continue to increase as well. In some fjord systems, the retreat of glaciers to locations with shallower grounding lines may reduce the impact of subglacial discharge on nutrient availability[6] — however, the grounding line depth at SK remains > 800 m below sea level for 10's of km inland of the current ice front[30], which will yield high nutrient entrainment rates and associated productivity induced by subglacial discharge in the future. This increase in phytoplankton growth has several implications for marine ecosystems around Greenland. First, changes in nutrient concentrations from glacier forcing may lead to future changes in phytoplankton community composition. Observations in Nuup Kangerlua, south of Qeqertarsuup Tunua, show that phytoplankton types vary with nutrient fluxes from the ice sheet[31,32] and glacier retreat[15]. This shift in composition is supported by the results of our high-discharge simulations in which we observe enhanced productivity in diatoms, picoeukaryotes, and picocyanobacteria. Second, since phytoplankton growth forms the base of the marine food web, spatial and temporal perturbations in productivity impact grazing by zooplankton and subsequently by fish populations such as Greenland halibut and other socio-economically important fishes in Greenland — fish

populations which are associated with productivity in fjords with high rates of subglacial discharge from deep, marine-terminating glaciers[14]. Relatedly, these changes in productivity and fish populations have the potential to induce downstream impacts on large marine mammals in Greenland, such as ringed seals, narwhals, and polar bears that use fjords as seasonal habitats and hunting grounds[33–35].

Looking to the future, there are several key measurements required to understand ecosystem changes now and in the coming decades. Additional measurements of nutrient availability are required to constrain model results, especially in coastal regions and fjords, which are hotspots of productivity yet often devoid of biogeochemical measurements. These additional measurements will allow a better determination of nutrient limitations in fjords around Greenland and offer insight into how they will respond to enhanced ice-sheet melt in the future. In addition, a deeper understanding of phytoplankton community composition in the Arctic is required to diagnose how productivity will respond to physical changes in the marine environment. In our simulations, the phytoplankton ecosystem is represented by four functional groups, yet the observed phytoplankton community composition around Greenland is far more complex[36,37]. Observations from the recently-launched hyperspectral Plankton, Aerosol, Cloud, ocean Ecosystem (PACE) satellite offers promise for furthering knowledge of community composition in Greenland's coastal waters, but observations must be linked with in-situ measurements to constrain remote sensing algorithms[38], which are lacking in many regions. Remotely-sensed estimates of community composition may become important with increased productivity because some species of phytoplankton have shown to contribute to harmful algal blooms (HABs) in other Arctic systems — however, to date, there has been limited investigation of changing HAB risk in Greenland waters[39,40]. An improvement in these measurements

and observations is essential for our developing understanding of this rapidly-changing Arctic environment now and over the coming century.

Methods

Numerical Ocean Modeling

We use the MIT General Circulation Model[41] to simulate circulation in a series of downscaled model configurations focused on Qeqertarsuup Tunua. The physical model is coupled with a biogeochemical model[42] provided by the *Darwin* package in the open-source *darwin3* fork of MITgcm. The downscaling approach begins with the Estimating the Circulation and Climate of the Ocean (ECCO) consortium's ECCO-Darwin Version 5 biogeochemistry state estimate[21] to derive initial and boundary conditions and external surface-ocean forcing for the regional L1 model on the West Greenland continental shelf which is used, in turn, to construct conditions for the L2 fjord-scale model. In each downscaled step, the initial, external, and boundary conditions from the parent model are used to generate the child model. The external forcing conditions include 6-hourly air temperature, specific humidity, short- and longwave radiation, surface runoff, precipitation, and vector winds. The approach here expands on that from Wood et al. 2024[20] by applying the tracer downscale routines for temperature and salinity to the 31 biogeochemical tracers required for the *darwin* package. We describe the ECCO-Darwin configuration and our downscaled configurations in the following subsections.

Global ECCO-Darwin Set-up. The ECCO-Darwin 1992–2023 state estimate leverages the data-assimilative capabilities of the ECCO Version 5 Alpha state estimate (LLC 270,[43]), coupled with a biogeochemical model with parameters optimized using a Green's Functions approach[21,44]. The biogeochemical model adds 31 tracers to the simulation encompassing dissolved inorganic carbon, nutrients, plankton biomass, and dissolved and particulate organic matter. The Darwin ecology includes four large-to-small phytoplankton function types (diatoms, other large eukaryotes, picoeukaryotes, and picocyanobacteria) and two zooplankton types that graze preferentially on either the large eukaryotes or smaller phytoplankton. These taxa were formulated to approximate phytoplankton community composition in the global ocean including highly productive upwelling regions and oligotrophic regions of the gyres. In the version of ECCO-Darwin used for this study, sinking particles are remineralized into water column unless they reach the ocean floor, in which case they are removed from the system.

For its hydrodynamical model, the ECCO-Darwin simulation is constructed from the ECCOv5 Alpha state estimate[43] — a global simulation constructed in an iterative framework designed to minimize errors relative to available physical ocean observations[45]. At a 1/3° resolution, the global model does not resolve eddies, particularly in the Arctic ocean where the Rossby radius of deformation is less than 10 km[46] — instead, the advective transport of heat, salt, and biogeochemical tracers by eddies are parameterized using the GMRedi scheme[47,48]. While effective in the open ocean, the approach does not resolve variability on or across the shelf break in Greenland, an important control on water properties on continental shelf. For this reason, previous studies using ECCOv5 Alpha to quantify ocean variability in West Greenland have sampled the model off of the continental shelf where the solution is consistent with in situ observations rather than on the shelf in Qeqertarsuup Tunua[49]. Here, we construct a downscaled L1 eddy-permitting model for the Davis Strait and West Greenland shelf break region to quantify eddy transport in these regions before constructing our higher-resolution experiments in Qeqertarsuup Tunua.

Regional and Fjord-scale configurations. The downscaled modeling approach in our study occurs in two steps: one regional model encompassing the Labrador Sea and Baffin Bay (L1, Fig. 1a) and another fjord scale model in Qeqertarsuup Tunua (L2, Fig. 1b). These configurations were constructed using a downscaled model framework as described in Wood et al. 2024[20].

The L1 simulation is constructed on a curvilinear grid with a nominal, eddy-permitting resolution of 3–4 km. The bathymetry of the L1 model was developed as a subset of existing ECCO Lat-Lon-Cap 1080 grid which uses bathymetry derived from the International Bathymetry Chart of the Arctic Ocean Version 3[50] — a dataset that does not contain contemporary mapping of small-scale fjords but does represent the deep troughs on the continental shelf. The L1 simulation is run for 30 years from 1992–2021 at a timestep of 300 seconds. Sea ice is implemented with the *seaice* package and vertical mixing is parameterized using the KPP scheme[51].

The L2 simulations are constructed on a grid with a uniform 500 m horizontal grid spacing, computed in a polar stereographic projection (EPSG: 3413). The bathymetry of the L2 simulation is derived from BedMachine[52] Version 5 and thus resolves fjords and includes realistic glacier grounding line depths. Additional vertical grid cells are added to this model to resolve mixing and biogeochemical processes in the photic zone, with the top grid cell being 1 meter thick and telescoping with depth. All of the packages and parameterizations in L2 are identical to those used in L1 with the exception of the biharmonic viscosity coefficient, which was increased from 1.5 in L1 to 2.15 in L2 — consistent with other models of similar resolution from the ECCO consortium. The packages and parameterizations also pertain to the biogeochemical model which includes the traits of phytoplankton community groups as defined in the global ECCO-Darwin solution[21]. Each L2 simulation is run from July 1 of the preceding year providing a 6-month spin-up period; then on 1 Jan, the experiments begin in two separate runs with and without glacier forcing. All model parameters, external forcings, initial conditions, and boundary conditions are kept consistent between the model experiments except for subglacial discharge and submarine melt, which is implemented with the *iceplume* package[23] that estimates the effect of subglacial discharge on glacier melt and upwelling in the fjord. Melt is computed on the glacier face using updated turbulent transfer coefficients from Schulz et al. 2022[53]. The iceplume is implemented using estimates of subglacial discharge from the MARv3.11 model, which has been hydrologically routed to outlets at the ice sheet boundary[54]. We classify all outlets within 5 km of each glacier boundary as subglacial discharge if the outlet depth is greater than 20 m below sea level, assuming that these outlets would be routed through cracks and moulins to the ice sheet bed. Subglacial discharge is implemented as distilled fresh water, i.e., the concentration of salinity and all nutrients are assumed to be zero. Discharge temperature is assumed to be 0 °C.

Partitioning ocean carbon uptake. We partition the total atmospheric carbon uptake (C_{total}) in Qeqertarsuup Tunua into four effects: the solubility of carbon dioxide (C_{sol}), the change in carbon dioxide solubility associated with temperature, salinity, and dissolved carbon changes from the subglacial discharge plume ($C_{sol,sg}$), the change in carbon flux induced by carbon fixation by primary producers (C_{pp}), and the additional change in carbon flux associated with changes in primary productivity induced by nutrient changes via plume-driven upwelling ($C_{pp,sg}$), i.e., $C_{total} = C_{sol} + C_{sol,sg} + C_{pp} + C_{pp,sg}$ To quantify each component of this partition, we run a suite of sensitivity experiments. To start, we turn off primary productivity to quantify C_{sol} and $C_{sol,sg}$. The first term C_{sol} is the carbon flux without the plume implementation. The second term $C_{sol,sg}$ is the difference between the model run with the plume and C_{sol}. Next, we turn on the primary producers to estimate C_{pp} and $C_{pp,sg}$. We establish C_{pp} as the difference between the model run with primary producers and that without (C_{sol}) in the absence of the plume. Finally, we quantify $C_{pp,sg}$ as the total carbon flux with both the plume and the primary producers, minus each of the effects above, i.e., as the residual calculation $C_{pp,sg} = C_{total} - C_{sol} - C_{sol,sg} - C_{pp}$. We assume that this linear decomposition holds because primary production does not affect temperature and salinity, which are the main drivers of changes in solubility, especially later in the season when CO_2 fluxes are largest.

Observations

To evaluate our simulations, we use a suite of remotely-sensed and in-situ data. For remote sensing, we use estimates of Chl-a as well as sea-ice

concentration data. Chl-a data was sourced from the daily, 1 km resolution Ocean Colour Climate Change Initiative (OC-CCI) Chl-a dataset, Version 6.0[55]. We interpolate the OC-CCI Chl-a dataset onto the 500-m resolution L2 model grid using bilinear interpolation. Sea-ice concentration in Qeqertarsuup Tunua was derived from daily passive microwave sensors and computed with the NASA Teams algorithm[56]. For in-situ observations, we compared our L1 model results with temperature, salinity, and heat flux measurements from the Davis Strait mooring array[57] (Supplementary Fig. 14) and our L2 Qeqertarsuup Tunua model results with temperature, salinity, and nutrient data available in and around Qeqertarsuup Tunua. For temperature and salinity, we used data from two autonomous profiling floats F9313 and F10052 deployed on 21 August 2022 and 19 August 2023, respectively. As these floats are not tethered or moored, they drift with currents in Qeqertarsuup Tunua when they are ascending or descending from the ocean bottom. As a result, we sample our model temperature and salinity results at the closest space-time GPS locations of the floats when they transmit profiles via satellite communication (Supplementary Fig. 15). For nutrient profiles, we collected all available nitrate and phosphate data in Qeqertarsuup Tunua from the World Ocean Database collected since 2000[58] and aggregated all data into a single space-time mean profile (Supplementary Fig. 12). This query yielded nutrient profiles in Qeqertarsuup Tunua in select years from 2004 to 2017.

Model evaluation against observations

Temperature and Salinity. In comparison to the Davis Strait mooring array, our L1 model shows a close consistency with mean temperature observations, particularly on the eastern side of the strait at depths of 200-500 m (Supplementary Fig. 14). This region is the location of the West Greenland Current (WGC) which advects ocean heat and other properties northward toward Qeqertarsuup Tunua. In the strait as a whole, the L1 model differences with observations range from $-2\,°C$ to $+2\,°C$ but in the WGC, biases are near-zero, giving confidence that the L1 model is resolving processes modulating temperature in this key current system. The L1 simulation also resolves the seasonal variability and approximate magnitude of northward heat transport in the WGC as measured by the Davis Strait mooring array[57] (Supplementary Fig. 14). The resolution of this northward heat transport and variability is key for reproducing variability upstream in Qeqertarsuup Tunua. As a result, the L2 model (which is forced on its boundary by the L1 model) reproduces both the magnitude and seasonal variability of temperature and salinity compared with observations in Qeqertarsuup Tunua (Supplementary Fig. 15). Seasonally, simulated temperature and salinity are consistent with the seasonal cycle measured by recently-deployed Argo floats on the shelf in Qeqertarsuup Tunua (Supplementary Fig. 15): between January and April, the thermocline and halocline shoal while during summer surface waters become warmer and fresher, coincident with the melting of sea ice and increased solar radiation reaching surface waters. Interannually, the magnitudes of deep Atlantic-sourced water are consistent with conductivity-temperature-depth data at depths of 200–250 m[49]. Namely, the year 2012 was the warmest of the years simulated, followed by 2008, 2019, and 2017. In effect, the downscaled model framework is generally able to replicate many of the observed hydrographic features of the Qeqertarsuup Tunua system.

Sea ice. In comparison with remotely-sensed estimates of sea-ice concentration, ice is present for approximately one month too long in all simulations, diminishing rapidly in May–June rather than April–May (Supplementary Fig. 13). Further, sea ice reforms at the start of December in the simulations rather than the start of January in observations. These model-data differences are likely due to incorrect, untuned, or unoptimized model parameters. Nonetheless, the model simulates real-world open water conditions during June–October when subglacial discharge and phytoplankton growth is prevalent. Therefore, we focus on the open-water season when the effect of glaciers on productivity is expected to be most prevalent.

Nutrients. Nutrient concentrations are not measured consistently in in our model regions but there are several years of observations available from the World Ocean Database[58] in Qeqertarsuup Tunua since 2000. To compare our model results with observations, we compute the mean nitrate and phosphate profiles from the model simulations and visualize differences from observations (Supplementary Fig. 12). We find that the modeled surface profiles of both macronutrients have a similar magnitude compared to observations in the photic zone although the models tend to biased low at depths greater than 100–200 m. This low bias is inherited from biases and unresolved transport processes in the ECCO-Darwin and L1 parent models used to initialize the L2 model. We did not attempt to bias-correct the nitrate and phosphate concentrations prior to running our L2 model because we did not have enough in situ data to quantify biases in the other chemical constituents such as nitrite, ammonium, and iron. We did not find sufficient publicly-available data for silica or iron during the years of our model simulations for a model-data comparison.

Chlorophyll-a. To assess our model results for Chl-a relative to observations, we compare our results with the OC-CCI V6 product from remotely-sensed data as well as in-situ measurements collected during an oceanographic cruise in 2022. Assessing estimates of Chl-a from remotely-sensed data products is difficult for three reasons: 1) the signals are integrated from an unknown depth to the surface, depending on the turbidity of the water; 2) algorithms in products like OC-CCI are derived using a global dataset of chlorophyll-a which has a strong sampling bias in the subtropics (i.e. away from the Arctic and the coast); and 3) other constituents in the water such as colored dissolved organic matter (CDOM) absorb in some of the same portions of the visible spectrum, which may bias the signal, particularly next to the coastline. For these reasons, we assess our modeled estimates of Chl-a compared to the relative spatial distribution and magnitudes of remotely-sensed estimates rather than absolute magnitudes. Figure 4 provides a spatial view of the comparison at a single depth (20 m) revealing similar magnitudes and spatial patterns to the OC-CCI product. However, there are some discrepancies near the coastline of Qeqertarsuup and the town of Aasiaat which may be the result of CDOM or other turbid constituents in shallow coastal zones influenced by terrestrial runoff. For an in-situ comparison, we use underway Chl-a data obtained from an EXO-1 (YSI Sonde) sensor at 2-minute intervals throughout the GLICE cruise from a water flow provided by a towfish at 2 m depth[17] (Supplementary Fig. 5). Sensor data below 0.01 RFU were assumed to be below detection. A 6-point Chl-a calibration was undertaken by comparing sensor fluorescence (RFU) to Chl-a concentrations measured on filters collected from the same towfish supply. Manual Chl-a samples were filtered (Whatman GF/F, 0.7 μm), extracted in 10 mL 96% ethanol for 24 h, and chlorophyll a fluorescence in the filtrate was then analyzed (TD-700, Turner Designs fluorometer) before and after the addition of 200 μL 1 M HCl. A linear regression produced a reasonable fit (R^2=0.88) with the formula: Chl-a (ng L^{-1}) = 182.4(YSI fluorescence)-27. From this comparison, we find that modeled values are similar to in situ observations in both magnitude and spatial distribution with higher concentrations in Sullorsuaq, upstream of the glaciers, compared to values in the center of Qeqertarsuup Tunua.

Data availability

Here, we list the online locations where the data sets can be accessed in the order that they are listed in the Methods section. The OC-CCI V6 chlorophyll concentration data[55] is available on the Ocean Colour browser at https://www.oceancolour.org/browser/. The passive microwave sea ice concentration data[56] is available at the National Snow and Ice Data Center at https://nsidc.org/data/g02202/versions/4. The Davis Strait mooring array data[57] is available on the Arctic Data portal at https://arcticdata.io/catalog/portals/DSOS/Data. The Argo float data[59] from Disko Bay is accessible on the NASA Earthdata portal at https://search.earthdata.nasa.gov/search/granules?p=C2491772150-POCLOUD.

The World Ocean Database profiles are accessible at https://www.ncei. noaa.gov/products/world-ocean-database. The subglacial discharge estimates which have been hydrologically routed to the coastline from the MAR regional climate model are available at https://dataverse.geus.dk/dataverse/freshwater. Output from the ECCO Darwin model is available on the ECCO drive: https://data.nas.nasa.gov/ecco/eccodata/llc_270/ecco_darwin_v5/output/. The in situ chlorophyll-a concentration data is located at https://emodnet.ec.europa.eu/en/data-ingestion. The data from the L1 and L2 models used for the analysis in this manuscript can be readily reproduced using the code provided in the Code Availability statement above. The processed model and data fields used to generate the figures in this manuscript are archived along with their accompanying scripts at https://doi.org/10.5281/zenodo.15858160.

Code availability

The modeling component of this study was conducted with the darwin3 fork of the MIT General Circulation Model[41], available at https://github.com/darwinproject/darwin3. The model configuration files for the ECCO-Darwin v5 model are available on the Darwin Github repository: https://github.com/MITgcm-contrib/ecco_darwin/tree/master/v05/llc270. The model configuration files for the L1 and L2 models derived from ECCO-Darwin in this study are archived at https://doi.org/10.5281/zenodo.15858160 and are available here: https://github.com/mhwood/downscale_ecco_v5_darwin.

References

1. Mouginot, J. et al. Forty-six years of Greenland Ice Sheet mass balance from 1972 to 2018. *Proc. Natl Acad. Sci.* **116**, 9239–9244 (2019).
2. Slater, D. et al. Characteristic Depths, Fluxes, and Timescales for Greenland's Tidewater Glacier Fjords From Subglacial Discharge-Driven Upwelling During Summer. *Geophys. Res. Lett.* **49**, e2021GL097081 (2022).
3. Carroll, D. et al. Subglacial discharge-driven renewal of tidewater glacier fjords. *J. Geophys. Res.: Oceans* **122**, 6611–6629 (2017).
4. Cape, M. R., Straneo, F., Beaird, N., Bundy, R. M. & Charette, M. A. Nutrient release to oceans from buoyancy-driven upwelling at Greenland tidewater glaciers. *Nat. Geosci.* **12**, 34–39 (2019).
5. Oliver, H. et al. Greenland subglacial discharge as a driver of hotspots of increasing coastal chlorophyll since the early 2000s. *Geophys. Res. Lett.* **50**, e2022GL102689 (2023).
6. Hopwood, M. J. et al. Non-linear response of summertime marine productivity to increased meltwater discharge around Greenland. *Nat. Commun.* **9**, 3256 (2018).
7. Hopwood, M. J. et al. How does glacier discharge affect marine biogeochemistry and primary production in the Arctic? *Cryosphere* **14**, 1347–1383 (2020).
8. Oliver, H., Castelao, R. M., Wang, C. & Yager, P. L. Meltwater-enhanced nutrient export from Greenland's glacial fjords: A sensitivity analysis. *J. Geophys. Res.: Oceans* **125**, e2020JC016185 (2020).
9. Ardyna, M. et al. Recent Arctic Ocean sea ice loss triggers novel fall phytoplankton blooms. *Geophys. Res. Lett.* **41**, 6207–6212 (2014).
10. Zhao, H., Matsuoka, A., Manizza, M. & Winter, A. Recent Changes of Phytoplankton Bloom Phenology in the Northern High-Latitude Oceans (2003-2020). *J. Geophys. Res.: Oceans* **127**, https://doi.org/10.1029/2021JC018346 (2022).
11. Manizza, M., Carroll, D., Menemenlis, D., Zhang, H. & Miller, C. E. Modeling the Recent Changes of Phytoplankton Blooms Dynamics in the Arctic Ocean. *J. Geophys. Res.: Oceans* **128**, e2022JC019152 (2023).
12. Hofer, S. et al. Greater Greenland Ice Sheet contribution to global sea level rise in CMIP6. *Nat. Commun.* **11**, 6289 (2020).
13. Juul-Pedersen, T. et al. Seasonal and interannual phytoplankton production in a sub-Arctic tidewater outlet glacier fjord, SW Greenland. *Mar. Ecol. Prog. Ser.* **524**, 27–38 (2015).
14. Meire, L. et al. Marine-terminating glaciers sustain high productivity in Greenland fjords. *Glob. Change Biol.* **23**, 5344–5357 (2017).
15. Meire, L. et al. Glacier retreat alters downstream fjord ecosystem structure and function in Greenland. *Nat. Geosci.* **16**, 671–674 (2023).
16. Kanna, N. et al. Upwelling of macronutrients and dissolved inorganic carbon by a subglacial freshwater driven plume in Bowdoin Fjord, northwestern Greenland. *J. Geophys. Res.: Biogeosciences* **123**, 1666–1682 (2018).
17. Hopwood, M. J. et al. A close look at dissolved silica dynamics in Disko Bay, west Greenland. *Glob. Biogeochemical Cycles* **39**, e2023GB008080 (2025).
18. Møller, E. F. et al. The sensitivity of primary productivity in Disko Bay, a coastal Arctic ecosystem, to changes in freshwater discharge and sea ice cover. *Ocean Sci.* **19**, 403–420 (2023).
19. Hoshiba, Y., Matsumura, Y., Kanna, N., Ohashi, Y. & Sugiyama, S. Impacts of glacial discharge on the primary production in a Greenlandic fjord. *Sci. Rep.* **14**, 15530 (2024).
20. Wood, M. et al. Decadal evolution of ice-ocean interactions at a large East Greenland glacier resolved at fjord scale with downscaled ocean models and observations. *Geophys. Res. Lett.* **51**, e2023GL107983 (2024).
21. Carroll, D. et al. The ECCO-Darwin data-assimilative global ocean biogeochemistry model: Estimates of seasonal to multidecadal surface ocean pCO2 and air-sea CO2 flux. *J. Adv. Modeling Earth Syst.* **12**, e2019MS001888 (2020).
22. Carroll, D. et al. Attribution of space-time variability in global-ocean dissolved inorganic carbon. *Glob. Biogeochemical Cycles* **36**, e2021GB007162 (2022).
23. Cowton, T., Slater, D., Sole, A., Goldberg, D. & Nienow, P. Modeling the impact of glacial runoff on fjord circulation and submarine melt rate using a new subgrid-scale parameterization for glacial plumes. *J. Geophys. Res.: Oceans* **120**, 796–812 (2015).
24. Krause, J. W. et al. Silicic acid limitation drives bloom termination and potential carbon sequestration in an Arctic bloom. *Sci. Rep.* **9**, 8149 (2019).
25. Slater, D. A. et al. Twenty-first century ocean forcing of the Greenland ice sheet for modelling of sea level contribution. *Cryosphere* **14**, 985–1008 (2020).
26. Maar, M. et al. Longer ice-free conditions and increased run-off from the ice sheet will impact primary production in Young Sound, Greenland. *J. Geophys. Res.: Biogeosciences* **130**, e2024JG008468 (2025).
27. Andresen, C. S. et al. Sediment discharge from Greenland's marine-terminating glaciers is linked with surface melt. *Nat. Commun.* **15**, 1332 (2024).
28. Krause, J. et al. The macronutrient and micronutrient (iron and manganese) content of icebergs. *Cryosphere* **18**, 5735–5752 (2024).
29. Neshyba, S. Upwelling by icebergs. *Nature* **267**, 507–508 (1977).
30. An, L. et al. Bed elevation of Jakobshavn Isbræ, West Greenland, from high-resolution airborne gravity and other data. *Geophys. Res. Lett.* **44**, 3728–3736 (2017).
31. Meire, L. et al. High export of dissolved silica from the Greenland Ice Sheet. *Geophys. Res. Lett.* **43**, 9173–9182 (2016).
32. Krawczyk, D. et al. Seasonal succession, distribution, and diversity of planktonic protists in relation to hydrography of the Godthåbsfjord system (SW Greenland). *Polar Biol.* **41**, 2033–2052 (2018).
33. Laidre, K. L. et al. Glacial ice supports a distinct and undocumented polar bear subpopulation persisting in late 21st-century sea-ice conditions. *Science* **376**, 1333–1338 (2022).

34. Laidre, K. L. et al. Narwhal (Monodon monoceros) associations with Greenland summer meltwater release. *Ecosphere* **15**, e70024 (2024).

35. Sakuragi, Y., Rosing-Asvid, A., Sugiyama, S. & Mitani, Y. Seasonal habitat use of ringed seals in the Thule area, northwestern Greenland. *Polar Sci.* **43**, 101145 (2024).

36. Krawczyk, D. W. et al. Microplankton succession in a SW Greenland tidewater glacial fjord influenced by coastal inflows and run-off from the Greenland Ice Sheet. *Polar Biol.* **38**, 1515–1533 (2015).

37. Elferink, S. et al. Molecular diversity patterns among various phytoplankton size-fractions in West Greenland in late summer. *Deep Sea Res. Part I: Oceanographic Res. Pap.* **121**, 54–69 (2017).

38. Lewis, K., Van Dijken, G. & Arrigo, K. R. Changes in phytoplankton concentration now drive increased Arctic Ocean primary production. *Science* **369**, 198–202 (2020).

39. Baggesen, C. et al. Molecular phylogeny and toxin profiles of Alexandrium tamarense (Lebour) Balech (Dinophyceae) from the west coast of Greenland. *Harmful Algae* **19**, 108–116 (2012).

40. Richlen, M. L. et al. Distribution of Alexandrium fundyense (Dinophyceae) cysts in Greenland and Iceland, with an emphasis on viability and growth in the Arctic. *Mar. Ecol. Prog. Ser.* **547**, 33–46 (2016).

41. Marshall, J., Adcroft, A., Hill, C., Perelman, L. & Heisey, C. A finite-volume, incompressible Navier Stokes model for studies of the ocean on parallel computers. *J. Geophys. Res.: Oceans* **102**, 5753–5766 (1997).

42. Brix, H. et al. Using Green's Functions to initialize and adjust a global, eddying ocean biogeochemistry general circulation model. *Ocean Model.* **95**, 1–14 (2015).

43. Zhang, H., Menemenlis, D. & Fenty, I. ECCO LLC270 ocean-ice state estimate (2018).

44. Menemenlis, D., Fukumori, I. & Lee, T. Using Green's functions to calibrate an ocean general circulation model. *Monthly weather Rev.* **133**, 1224–1240 (2005).

45. Forget, G. et al. ECCO version 4: An integrated framework for non-linear inverse modeling and global ocean state estimation. *Geoscientific Model Dev.* **8**, 3071–3104 (2015).

46. Nurser, A. & Bacon, S. The rossby radius in the Arctic Ocean. *Ocean Sci.* **10**, 967–975 (2014).

47. Redi, M. H. Oceanic isopycnal mixing by coordinate rotation. *J. Phys. Oceanogr.* **12**, 1154–1158 (1982).

48. Gent, P. R., Willebrand, J., McDougall, T. J. & McWilliams, J. C. Parameterizing eddy-induced tracer transports in ocean circulation models. *J. Phys. Oceanogr.* **25**, 463–474 (1995).

49. Khazendar, A. et al. Interruption of two decades of Jakobshavn Isbrae acceleration and thinning as regional ocean cools. *Nat. Geosci.* **12**, 277–283 (2019).

50. Jakobsson, M. et al. The international bathymetric chart of the Arctic Ocean (IBCAO) version 3.0. *Geophys. Res. Lett.* **39**, https://doi.org/10.1029/2012GL052219 (2012).

51. Large, W. G., McWilliams, J. C. & Doney, S. C. Oceanic vertical mixing: A review and a model with a nonlocal boundary layer parameterization. *Rev. geophysics* **32**, 363–403 (1994).

52. Morlighem, M. et al. BedMachine v3: Complete bed topography and ocean bathymetry mapping of Greenland from multibeam echo sounding combined with mass conservation. *Geophys. Res. Lett.* **44**, 11–051 (2017).

53. Schulz, K., Nguyen, A. & Pillar, H. An improved and observationally-constrained melt rate parameterization for vertical ice fronts of marine terminating glaciers. *Geophys. Res. Lett.* **49**, e2022GL100654 (2022).

54. Mankoff, K. D. et al. Greenland liquid water discharge from 1958 through 2019. *Earth Syst. Sci. Data* **12**, 2811–2841 (2020).

55. Sathyendranath, S. et al. ESA ocean Colour climate change initiative (Ocean_Colour_cci): Version 6.0 Data. *(No Title)* (2023).

56. Meier, W. N., Fetterer, F., Windnagel, K. A. & Stewart, J. S. NOAA/NSIDC Climate Data Record of Passive Microwave Sea Ice Concentration. (G02202, Version 4, Date Accessed 12-05-2024) (2021).

57. Curry, B., Lee, C. M., Petrie, B., Moritz, R. E. & Kwok, R. Multiyear Volume, Liquid Freshwater, and Sea Ice Transports through Davis Strait, 2004-10. *Section: Journal of Physical Oceanography* (2014).

58. Garcia, H. E. et al. World Ocean Atlas 2023, Volume 4: Dissolved Inorganic Nutrients (Phosphate, Nitrate, and Silicate) (2024).

59. OMG. Ocean water properties data from alamo floats version 1 https://podaac.jpl.nasa.gov/dataset/OMG_L1_FLOAT_ALAMO (2022).

Acknowledgements

Author contributions

M.W. conceived of the experiments, ran the downscaled models, analyzed the results, lead writing the manuscript and obtained funding for the study. D.C. helped designed the experiments and ran the global model. I.F. supported the numerical implementation of the model downscaling. C.B. assisted with the analysis of nutrient limitation across phytoplankton functional groups. B.D. analyzed the physics of the L1 model and its consistency with observations. S.D. assisted with the implementation of the darwin package and the interpretation of nutrient limitation. M.H. assisted with the interpretation of modeled nutrient concentrations in comparison to in-situ observations. A.K. helped conceive of the downscaled model approach. L.M. assisted with the interpretation of model results in Qeqertarsuup Tunua. H.O. helped with the assessment of the study design and comparison to in-situ observations. T.P. collected remotely-sensed estimates of chlorophyll-a and assisted with the analysis. J.W. helped with the comparison to ocean observations in Qeqertarsuup Tunua. All authors contributed to reviewing and editing the manuscript.

Competing interests

The authors declare no competing interests.

Additional information

Supplementary information The online version contains supplementary material available at https://doi.org/10.1038/s43247-025-02599-1.

Correspondence and requests for materials should be addressed to Michael Wood.

Peer review information *Communications Earth & Environment* thanks the anonymous reviewers for their contribution to the peer review of this work. Primary Handling Editors: Ilka Peeken and Alice Drinkwater. A peer review file is available.

Reprints and permissions information is available at http://www.nature.com/reprints